Materials Science & Engineering A 680 (2017) 64–74

Contents lists available at ScienceDirect

Materials Science & Engineering A

journal homepage: www.elsevier.com/locate/msea

# Effects of Sb micro-alloying on precipitate evolution and mechanical properties of a dilute Al-Sc-Zr alloy

Jeffrey D. Lin[a,*], Philipp Okle[a,1], David C. Dunand[a], David N. Seidman[a,b]

[a] Northwestern University, Department of Materials Science and Engineering, Evanston, IL 60208-3108, USA
[b] Northwestern University Center for Atom-Probe Tomography, Northwestern University, 2220 Campus Drive, Evanston, IL 60208-3108, USA

ARTICLE INFO

*Keywords:*
Aluminum
Scandium
Zirconium
Alloys
$L1_2$
Precipitation

ABSTRACT

An Al-Sc-Zr aluminum alloy with Sb micro-addition (Al-0.066Sc-0.050Zr-0.021Sb at%) is cast and heat-treated to study the effects of Sb on the nucleation, growth, coarsening kinetics and precipitate morphology, and resulting mechanical properties at ambient and elevated temperatures. When isochronally aged, the Sb-containing alloy exhibits a peak microhardness (607 ± 12 MPa) at 475 °C, which is greater than that of a comparable Sb-free alloy at the same temperature (549 ± 17 MPa), and a smaller rate of decrease of microhardness values due to precipitate coarsening for aging temperatures > 475 °C. When isothermally aged, the Sb-containing alloy achieves larger peak microhardness values at 300 °C for more than a month (~80 MPa difference) and 400 °C for ~8 h (~200 MPa difference) than the Sb-free alloy. Atom-probe tomography of the peak-aged Sb-containing alloy demonstrates that Sb partitions to the precipitates, and is enriched in the Zr-rich shell (up to 0.35 at% Sb). For creep testing at 300 °C, the Sb-containing alloy exhibits smaller steady-state strain-rates than the Sb-free control alloy at applied stresses > 15 MPa. It is hypothesized that the effects of Sb micro-alloying (partitioning to precipitates, enhanced precipitate coarsening and higher creep resistance) are linked with the following mechanisms: (i) enhanced Zr diffusion in the matrix due to attractive Sb-Zr interactions; (ii) reduction in matrix/precipitate interfacial free energy, when Sb is present; and (iii) an increase in precipitate/matrix lattice parameter mismatch resulting in stronger elastic interactions with dislocations.

## 1. Introduction

Precipitation-strengthened aluminum alloys microalloyed with scandium and zirconium have been developed as a promising family of lightweight alloys for use at temperatures as high as 400 °C, with applications in aerospace and automotive structural components [1–10]. Current, traditional age-hardened aluminum alloys cannot to be used at high temperatures for long times since the precipitate coarsen rapidly above ~230 °C, thereby weakening the alloy [11–16]. Scandium and zirconium form nanoscale trialuminide $Al_3X$ (X=Sc or Zr) precipitates with the $L1_2$ structure, which are coherent with the face-centered cubic (f.c.c.) crystal structure of aluminum, and displays slow coarsening rates due to the diffusion of Sc and Zr in Al [1,17–30]. Scandium has the greatest ability to strengthen aluminum on a per atom basis by grain refinement and formation of ordered ($L1_2$ -structure) nanoscale precipitates that are stable after prolonged aging at 300 °C [17,18,22–25,27,31–34]. Zirconium forms metastable $L1_2$ precipitates, which are coarsening-resistant at temperatures below 500 °C, before transforming to the $D0_{23}$ tetragonal structure [19,21,29,35–38].

Combining Sc and Zr in aluminum yields an alloy with $L1_2$ $Al_3(Sc, Zr)$ precipitates, displaying superior heat-resistance and high strength [33,39–46]. Precipitates with a core-shell morphology are formed in these alloys during aging, where the core is Sc-rich and the shell is Zr-rich due to Scandium's higher diffusivity, and thus its earlier precipitation in aluminum [3,10,39,40,47–51]. The Zr-rich shell provides a smaller lattice parameter mismatch with the matrix, a diffusion barrier against Sc atoms, resulting in coherent $Al_3(Sc, Zr)$ precipitates with small coarsening rates at 400 °C for up to 2 mos. Recently, additional elements, such as erbium and silico, have been added to Al-Sc-Zr alloys and studied for their effects on precipitate morphology, nucleation and growth rates, coarsening resistance, and strengthening at ambient and elevated temperatures [47,52–54]. Erbium improves the creep resistance by the formation of a higher mismatching Er-rich inner core within the precipitates, Si accelerates the nucleation, growth and coarsening of the precipitates, and improves the peak strength achieved during thermal aging due to an attractive binding free energy between Si atoms and vacancies [47,52–55]. Booth-Morrison et al. [53] attribute the effects on the early stages of nucleation and growth of Sc-rich precipitate cores to: (i) the favorable formation of Sc-Si and Si-

* Corresponding author.
[1] Current address: Eidgenössische Technische Hochschule Zürich, Zurich, Switzerland.

http://dx.doi.org/10.1016/j.msea.2016.10.067
Received 18 July 2016; Received in revised form 5 October 2016; Accepted 12 October 2016
Available online 24 October 2016
0921-5093/

vacancy dimers, which decreases the migration energy of Sc in Al from 0.74 to 0.45 eV atom$^{-1}$ and increases the Sc diffusivity; and (ii) an attractive binding free energy between Si and vacancies leading to vacancy clusters that become heterogeneous nucleation sites for precipitates. Vo et al. [54] propose that the accelerated coarsening of the $Al_3$(Sc, Zr) precipitates is a result of Si atoms increasing the diffusivity of Sc within the Zr-rich regions in the precipitate, and also possibly Zr.

This article focuses on a study of an Al-Sc-Zr alloy with microalloying addition of Sb, which was selected based on Wolverton's [55] first-principle calculations of binding energies between solute atoms and vacancies in aluminum. Since Sb has a favorable 0.30 eV attractive binding energy, at 0 K, with nearest-neighbor vacancies in Al, we hypothesize that Sb will exhibit a similar effect to that of Si on accelerating the precipitation kinetics of $Al_3$(Sc, Zr) by binding favorably with Zr, as many intermetallic compounds form in the Sb-Zr binary phase [56]. The Al-Sb binary phase diagram indicates a very limited solid solubility of Sb in aluminum ( < 0.02 at% at 627 °C), with AlSb being the only intermetallic line-compound [57–59]. Although it is possible that the solubility of Sb in Al is altered as a result of Sc and Zr additions in the alloy, there currently exist no ternary phase diagrams for the Al-Sc-Sb or Al-Zr-Sb system. Furthermore, it is likely that the effects of Sc and Zr on the solubility of Sb in Al can be neglected due to the small amounts of Sc and Zr in the alloy ( < 0.1 at% for either). To disperse the Sb atoms throughout the Al solid-solution and reduce or prevent AlSb primary precipitates formation during solidification and homogenization, a very small concentration of Sb (200 ppm at%) was chosen. Herein, we compare a previously-studied Sb-free alloy to our new Sb-containing alloy with respect to aging kinetics, coarsening resistance, precipitate composition, and microhardness and creep resistance.

## 2. Materials and methods

### 2.1. Alloy preparation and heat treatment

A 200 g cylindrical ingot was cast in air for an alloy with a nominal atomic composition of Al-0.06Sc-0.06Zr-0.02Sb at% (Al-0.10Sc-0.21Zr-0.09Sb wt%) by melting pieces of 4N (99.99% purity) Al (Alcoa Inc.), Al-Sc and Al-Zr master alloys (Alcoa Inc.), and ~99.5% pure Sb (Alfa Aesar) in an alumina crucible at 800 °C. The melt was stirred vigorously before being poured into a graphite crucible placed onto an ice-cooled copper platen to encourage directional solidification, thereby preventing the formation of internal shrinkage cavities during solidification. Direct-current plasma optical-emission spectrometry (DCP-OES) was performed on ~0.50 g of the ingot by ATI Specialty Alloys and Components (Albany, OR), and the results are displayed in Table 1, alongside those measured utilizing local-electrode atom-probe (LEAP) tomography. The DCP determined concentrations for Sc, Zr and Sb are close to their nominal concentrations, and the former is used in the reminder of this article.

The cast alloy was homogenized in air at 640 °C for 3 days and then water-quenched, resulting in a supersaturated solid-solution. Samples of the ingot were cut and heat-treated sequentially from 100 to 575 °C with 25 °C/1 h steps for isochronal aging. Other samples were isothermally aged at 300 and 400 °C for times ranging from 0.5 to 2 months. Double isothermal aging (300 °C for 4 h and subsequently at 400 and 425 °C for 0.5 h to 1 week) was performed to develop a heat treatment sequence for maximum alloy strength with a minimal aging time. Vickers microhardness measurements were made using a Struers Duramin 5 hardness tester with 200 g load, dwell time of 5 s, and a magnification of 40×, while electrical conductivity measurements were performed using a Foerster SigmaTest 2.069 at frequencies of 120, 240, 480, and 960 kHz. Both microhardness and conductivity measurements were utilized to follow the time and temperature evolution of the precipitates.

### 2.2. Creep experiments

A constant load compressive creep experiment was performed at 300 ± 1 °C on a cylindrical specimen with a 10 mm diameter and a 20 mm height. The specimen had been isochronally aged to 450 °C after homogenizing at 640 °C for 72 h with a final aging temperature well above the creep temperature, to insure no aging during the creep test. The samples were heated in a three-zone furnace, with the temperature monitored using a thermocouple placed within ~1 cm of the specimen, which were placed between two boron-nitride coated alumina platens, and subjected to uniaxial compressive loads by Ni superalloy push-rods employing dead weights. Sample strain was determined by measuring the cross-head displacement using a linear-variable displacement-transducer (LVDT), with a resolution of ~6 μm, corresponding to a strain increment of ~$3\times10^{-4}$. The specimens were deformed at a constant load until steady-state (secondary) creep was achieved; the load was then increased and the measurement repeated. As a result, several creep rates for sequentially increasing applied stresses were measured from a single specimen without deforming the specimen more than 13%.

### 2.3. Microstructural imaging

Specimens for three-dimensional (3D) local-electrode atom-probe (LEAP) tomography were prepared by cutting blanks, with a diamond-blade precision saw, to dimensions of ~$0.45\times0.45\times10$ mm$^3$. The blanks were cut from samples aged isochronally to 450 °C utilizing 25 °C/1 h steps. They were then electropolished at room temperature by thinning the blanks at 25–20 V DC using a solution of 10% perchloric acid in acetic acid, followed by necking and final nanotip formation at 15–12 V DC with a solution of 2% perchloric acid in butoxyethanol [47,54]. Ultraviolet (UV) laser assisted APT was performed using a LEAP 4000Si-X tomograph (Cameca, Madison, WI) at a specimen temperature of 30 K, a UV laser energy of 25 pJ pulse$^{-1}$, and a pulse repetition rate of 500 kHz. The data were analyzed using IVAS reconstruction software (Cameca), and measurement errors were calculated using counting statistics and standard error propagation techniques.

A surface of the Al-Sc-Zr-Sb alloy specimen after homogenization at 640 °C was polished to a ~0.05 μm finish, and then etched with Keller's reagent to reveal the grains and dendritic structure. The images were recorded using a Nikon Eclipse MA200 optical microscope with bright- and dark-field modes. Additionally, the base surface of the creep specimen after aging isochronally to 450 °C was polished to a ~1 μm

**Table 1**
Compositions of the base and experimental alloys given in atomic percent (at%) determined by direct current plasma – optical emission spectroscopy (DCP-OES) and local electrode atom-probe (LEAP) tomography. The detection limit of each method is indicated for Si.

| Nominal composition | Measured composition from DCP-OES | | | | Measured composition from LEAP | | | |
|---|---|---|---|---|---|---|---|---|
| | Sc | Zr | Sb | Si | Sc | Zr | Sb | Si[a] |
| Al-0.06Sc-0.06Zr[21] | 0.067 | 0.052 | – | < 0.005 | 0.069 | 0.026 | – | < 0.002 |
| Al-0.06Sc-0.06Zr-0.02Sb | 0.066 | 0.050 | 0.021 | < 0.005 | 0.047 | 0.034 | < 0.002 | < 0.002 |

[a] Atomic concentration of $^{28}Si^{2+}$ atoms from LEAP tomography.

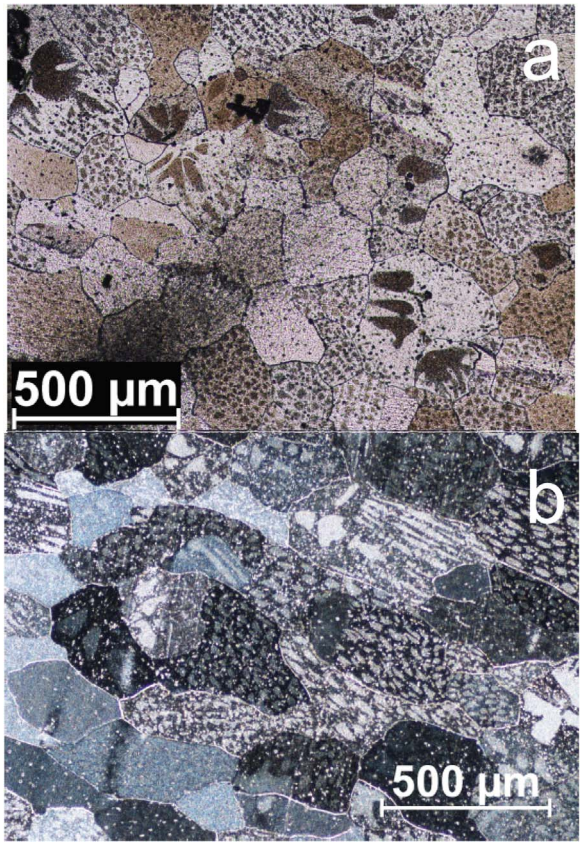


**Fig. 1.** Bright-field (a) and dark-field optical micrographs of etched cross-section of Al-0.06Sc-0.06Zr-0.02Sb at% in the homogenized state. Numerous dendrite arm cross-sections are observed within the grains of the specimen.

finish and then etched with Keller's reagent to reveal the grain boundaries.

## 3. Results

### 3.1. Dendrites and grain size

The micrographs of the Al-Sc-Zr-Sb alloy in the homogenized state, Fig. 1, indicate that there is a large volume fraction (~45%) of dendrite arm cross-sections within each grain. Dendrites form during alloy solidification and can lead to the development of precipitate-free regions among the dendrite arms, which can have deleterious effects on the mechanical properties [3,21]. A micrograph of the etched surface of the Sb-containing creep specimen, Fig. 2, indicates that a majority of the grains have lengths in excess of ~1 mm. Given the grain dimensions, applied compression loads (~13–30 MPa), and the testing temperature, 300 °C, we can safely state that the dominant creep mechanism is dislocation climb [60–62].

### 3.2. Isochronal aging

Fig. 3 displays the microhardness and conductivity values, as a function of isochronal aging temperature, for the Sb-free Al-Sc-Zr alloy and the new Sb-containing Al-Sc-Zr-Sb alloy. The data for the Sb-free alloy are from Booth-Morrison et al. [47]. The microhardness and conductivity values for the Sb-containing alloy remain relatively unchanged at 260 ± 7 MPa and 29.90 ± 0.05 MS/m, respectively, between 100 and 275 °C, indicating the absence of precipitation. The microhardness and conductivity start increasing at 300 °C, indicating the onset of precipitation and microhardness peaks at 375 °C at 560 ± 7 MPa, which corresponds to the precipitation of Sc atoms from the matrix to form Sc-rich $Al_3$(Sc, Zr) precipitates, based on the archival literature [3,18,19]. Similarly, the microhardness and conductivity values for the Sb-free Al-Sc-Zr alloy display very little change from their homogenized state values of ~200 MPa and ~31.50 MS/m, respectively, up to 275 °C, after which both increase significantly for aging temperatures between 300 and 350 °C.

Above 375 °C, the microhardness of the Sb-containing alloy increases slowly and peaks again at ~450 °C with values of 618 ± 13 MPa, which corresponds to the precipitation of Zr from the matrix, forming a Zr-rich $Al_3$(Zr, Sc) shell on the existing precipitates, as also reported in

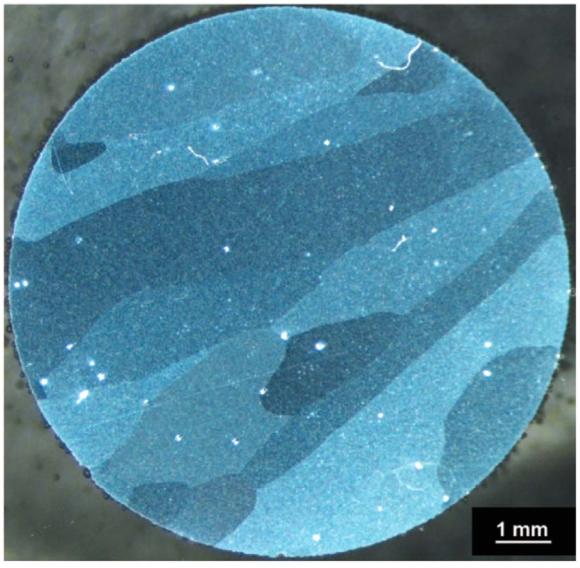


**Fig. 2.** Micrograph of the etched base surface of the creep specimen of an Al-0.06Sc-0.06Zr-0.02Sb at% alloy. The large grain diameters in the specimen indicate that dislocation creep is the dominant mechanism.

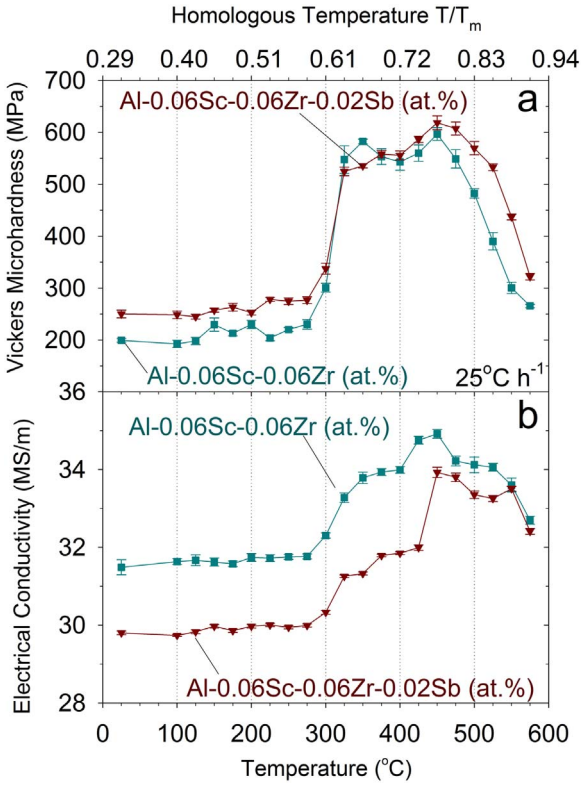


**Fig. 3.** Temporal evolution of the (a) Vickers microhardness and (b) electrical conductivity for the Sb-free[21] and Sb-containing alloys for isochronal aging.

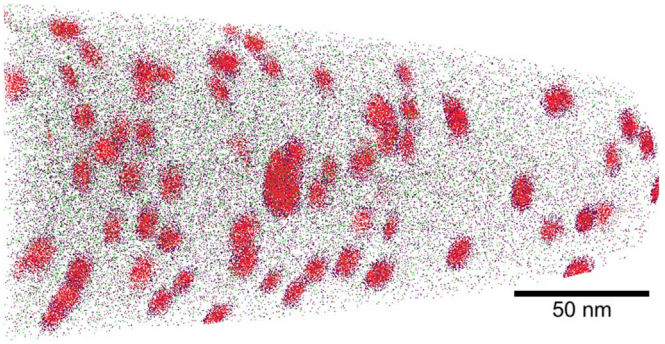


**Fig. 4.** Reconstruction of the Al-0.06Sc-0.06Zr-0.02Sb (at%) atom-probe tomographic nanotip taken from a sample isochronally aged to 450 °C after homogenizing at 640 °C for 72 h. The Sc atoms are in red, Zr atoms in purple, Sb atoms in light green, and Si atoms in black. The Al atoms have been omitted for the sake of clarity. (For interpretation of the references to color in this figure legend, the reader is referred to the web version of this article.)

Refs. [3,5,38]. By contrast, the microhardness and electrical conductivity for the Sb-free alloy decrease and plateau, respectively, between 350 and 400 °C, indicative of coarsening of the initially formed $Al_3Sc$ precipitates, and increase between 400 and 450 °C, as expected from precipitation of Zr from the matrix. The microhardness and conductivity values for both alloys decrease at aging temperatures above 450 °C due to the dissolution of the precipitates and the solutionizing of Sc, Zr and Sb atoms. Although the microhardness loss is significantly reduced for the new Al-Sc-Zr-Sb alloy when compared with the Sb-free alloy, as indicated by the consistently higher microhardness values for the former alloy at any given temperature > 450 °C. For example, at 550 °C (homologuous temperature of 0.88), the Sb-containing alloy (HV=437 ± 6 MPa) is much harder than the Sb-free alloy. In summary, it appears that Sb micro-additions neither affect significantly the precipitation of Sc from the matrix nor the first peak microhardness value achieved at 375 °C from these precipitates, but accelerates the precipitation of Zr between 350 and 450 °C, and decelerates the coarsening rate of core-shell $Al_3(Sc, Zr)$ precipitates above 450 °C, with a substantial microhardness of 437 ± 6 MPa maintained at 550 °C.

Fig. 4 displays a three-dimensional (3D) atomic-scale reconstruction of the Sb-containing alloy aged isochronally to 450 °C as obtained from APT. Table 2 presents a comparison of the precipitate number density, $N_v$, mean precipitate radius, $< R(t) >$, volume fraction, $\phi$, and microhardness values between the Al-Sc-Zr and Al-Sc-Zr-Sb alloy, which are calculated using the so-called cluster analysis (Cameca, Madison, WI). for the Sb-containing alloy is measured as $9.4 \pm 0.6 \times 10^{22}$ $m^{-3}$, which is more than four times the value measured by Booth-Morrison et al. [47] in the Sb-free Al-Sc-Zr alloy, the average precipitate radius is the same within error, and the volume fraction for the Al-Sc-Zr-Sb alloy is almost three times that of the Sb-free alloy.

Measurements of volume fraction and number density by LEAP tomography are susceptible to large statistical variations because the nanotips constitute a small volume, when compared to those probed

**Table 2**
Precipitate number density, $N_v$, mean precipitate radius, $< R >$, volume fraction of precipitates, ϕ, and Vickers microhardness value HV for the Sb-free[21] and Sb-containing alloys after homogenization at 640 °C for 72 h and isochronal aging up to 450 °C.

| Alloy | $N_v$ ($\times 10^{22}$ $m^{-3}$) | $< R >$ (nm) | $\phi$ (%) | HV (MPa) | Nanotip length (nm) |
|---|---|---|---|---|---|
| Al-Sc-Zr[21] | 2.1 ± 0.2 | 3.1 ± 0.4 | 0.251 ± 0.002 | 597 ± 12 | ~290 |
| Al-Sc-Zr-Sb | 9.4 ± 0.6 | 3.1 ± 0.7 | 0.70 ± 0.002 | 618 ± 13 | ~240 |

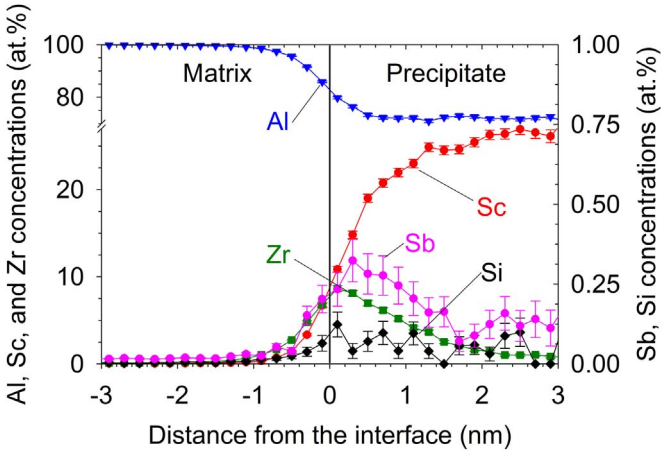


**Fig. 5.** Proximity histogram across the matrix-precipitate interface recorded for 63 precipitates within the atom-probe tomographic nanotip of an Al-0.06Sc-0.06Zr-0.02Sb at% sample aged isochronally to 450 °C after homogenizing at 640 °C for 72 h. The interface (x=0) is set at the inflection point of the Al concentration curve. The matrix is on the left-hand side and the precipitates are on the right-hand side of the vertical line indicating the position of the interface.

via microhardness and conductivity testing. Therefore, it is likely that the large differences in volume fraction and number density for the two alloys aged isochronally to 450 °C can be attributed to statistical variation, given that the microhardness of the alloy is within error the same. The precipitate radii are within error is consistent with the absence of a microhardness difference between the two alloys.

Fig. 5 displays concentration profiles for Al, Sc, Zr, Si, and Sb as a function of distance, where the x=0 point is placed at the inflection point of the Al curve, which defines the interface between the precipitate (right-hand side) and the solid-solution matrix (left-hand side). The concentration profiles are generated using the proximity histogram (proxigram) methodology [63] in the IVAS software package, which is based on 63 precipitates. While the amount of solute (Sc, Zr, Si, and Sb) in the matrix is negligible, the four elements are present within the precipitates. The peak concentration of Zr of ~8 at% is less than 0.25 nm from the interface, although there is still a sizeable concentration of Zr towards the center of the precipitate (~1 at%), which may be the result of the accelerated incorporation of Zr in the precipitates. The peak for Sc of ~25 at% is found at the precipitates centers based on measurements of $< R >$. These peak Zr- and Sc-concentrations correspond, respectively, to the Zr- and Sc-rich regions of the core-shell precipitates. A peak of 0.3 at% for Sb (compared to 0.02 at% for the nominal alloy composition) is found near the Zr-peak, indicating that Sb segregates largely to the Zr-rich shell. Nevertheless, a significant amount of Sb and Zr is found at the centers of the precipitates with constant concentrations of ~0.15 at% and ~1 at% respectively. By contrast, Si atoms appear to be distributed relatively evenly across the matrix-precipitate interface.

The composition of the overall APT nanotip, matrix, and the precipitates measured using APT on Sb-free and Sb-containing alloys samples aged isochronally to 450 °C are displayed in Table 3. While the DCP-OES results for both alloys (Table 1) match closely the target nominal compositions, the LEAP tomography measurements are taken from small sampling volumes that are prone to variations, as the nanotip may be taken from a solute-enriched dendrite or a solute-depleted interdendritic channel. The measured concentration of Zr in the precipitates is smaller for the Sb-containing alloy, probably because of its higher measured number density of precipitates, such that the Zr atoms are dispersed more sparsely between the precipitates.

### 3.3. Isothermal aging

The Vickers microhardness and electrical conductivity measure-

**Table 3**
The compositions, in atomic percent (at%), of the atom-probe tomograph nanotip, matrix, and precipitates for the Sb-free[21] and Sb-containing alloys homogenized at 640 °C for 72 h and isochronally aged through 450 °C as determined by LEAP tomography. The heating rate is 8 K $h^{-1}$.

| | Al-0.06Sc-0.06Zr[21] | | | | | Al-0.06Sc-0.06Zr-0.02Sb | | | | |
|---|---|---|---|---|---|---|---|---|---|---|
| | Al | Sc | Zr | Sb | Si[a] | Al | Sc | Zr | Sb | Si[a] |
| Overall nanotip | Balance | 0.069 | 0.026 | – | < 0.002 | Balance | 0.047 | 0.034 | < 0.002 | < 0.002 |
| Matrix | Balance | 0.016 | 0.013 | – | < 0.002 | Balance | < 0.002 | 0.011 | < 0.002 | < 0.002 |
| Precipitate | 71.95 | 22.63 | 5.42 | – | < 0.002 | 72.10 | 26.10 | 1.69 | 0.13 | 0.04 |

[a] Atomic concentration of $^{28}Si^{2+}$ atomic as determined by LEAP tomography.

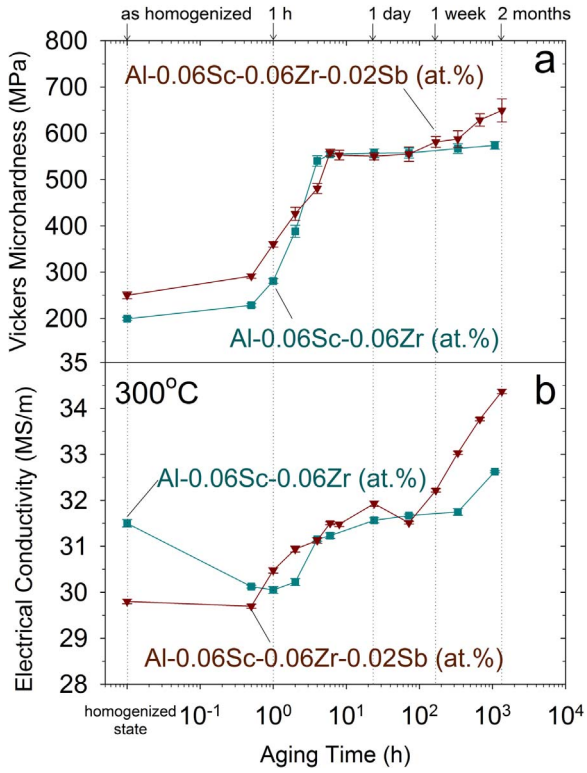


**Fig. 6.** Temporal evolution of the (a) Vickers microhardness and (b) electrical conductivity for the Sb-free[21] and Sb-containing alloys for isothermal aging at 300 °C.

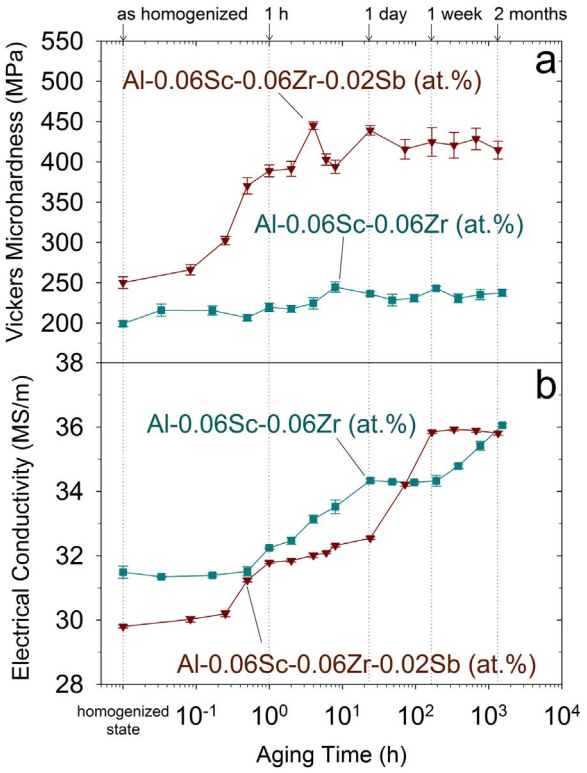


**Fig. 7.** Temporal evolution of the (a) Vickers microhardness and (b) electrical conductivity or the Sb-free[21] and Sb-containing alloys for isothermal aging at 400 °C.

ments, as a function of aging time, at a temperature of 300 °C is shown in Fig. 6 for the Al-Sc-Zr and Al-Sc-Zr-Sb alloys. The first notable increase in microhardness corresponds to the precipitation of Sc atoms out of the solid-solution matrix [47,53]. While the microhardness values for the new Al-Sc-Zr-Sb alloy are higher than that of the Sb-free alloy for aging times less than ~2 h, for longer aging times the microhardness values become similar. These results in concert with the isochronal aging curves indicate that Sb has very little effects on the precipitation of Sc out of the matrix. After reaching a microhardness of 550 ± 10 MPa and conductivity of 31.50 ± 0.05 MS/m after ~6 h of aging, these values for the Sb-containing alloy remain approximately constant for aging times up to 1 week. Both microhardness and conductivity subsequently increase as a result of Zr precipitation from the matrix [29,38]. After two months, the microhardness and conductivity for the Sb-containing alloy reaches 650 ± 25 MPa and 34.37 ± 0.05 MS/m, respectively, while the microhardness and conductivity measurements for the Sb-free alloy remain approximately unchanged. These results indicate that Sb accelerates the nucleation and growth of the Zr-rich shell of the $Al_3$(Sc, Zr) precipitates.

Fig. 7 shows the hardness and conductivity measurements as a function of time for isothermal aging at 400 °C. While the Sb-free alloy's hardness values remain roughly the same at a low value of ~230 MPa for aging times even beyond 2 months, the conductivity increases from 31.51 ± 0.14 MS/m to 34.30 ± 0.21 MS/m between 1 h and 2 days of aging, indicating precipitation of coarse Sc-rich precipitates from the matrix [47,53]. The conductivity plateaus until after two weeks of total aging are due to saturation of Sc atoms from matrix, and then increases again to 36.25 ± 0.05 MS/m after aging for 2 months, which corresponds to the precipitation of coarse Zr-rich precipitates from the solid-solution matrix [29,38].

After aging the Al-Sc-Zr-Sb alloy for 15 min, the microhardness and conductivity begin to increase as a result of nucleation and growth of small precipitates [64]. The first microhardness peak at 450 ± 5 MPa is reached after 4 h of aging, while the conductivity steadily increases to 32.55 ± 0.03 MS/m after aging for 1 d, as a result of Sc precipitation out of the matrix. The microhardness value decreases slightly between 4 and 24 h as a result of coarsening of the $Al_3Sc$ precipitates. The peak strength achieved at 400 °C is considerably smaller than that reached upon aging at 300 °C due to the smaller driving force for nucleation at higher aging temperatures, resulting in a smaller number density of coarser precipitates [65]. The next increase in conductivity to 35.90 ± 0.06 MS/m occurs between one day and two weeks of aging, as a result of Zr precipitation out of the matrix. The fact that this increase occurs earlier than for the Sb-free alloy again suggests that Sb accelerates the precipitation of Zr from the matrix. The microhardness is, however, unaffected, probably because weakening by coarsening negates

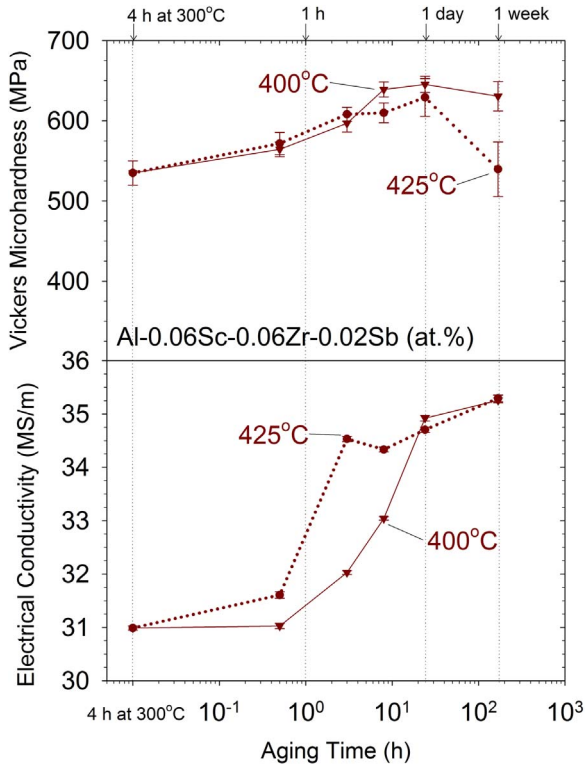


**Fig. 8.** Temporal evolution of the (a) Vickers hardness (b) and electrical conductivity measurements for the Sb-free[21] and Sb-containing alloys during isothermal aging at 400 °C and 425 °C, after prior aging at 300 °C for 4 h.

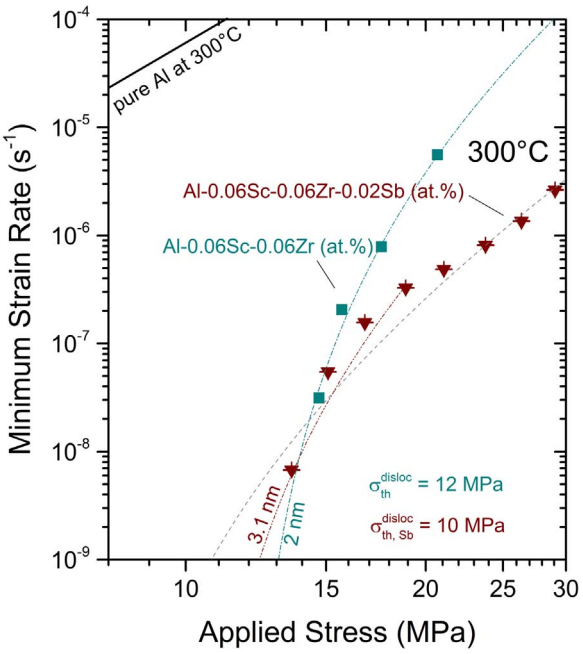


**Fig. 9.** Double-logarithmic plot of minimum creep rate vs. applied stress for compressive creep experiments at 300 °C for alloy is inferred from Knipling et al. [3]. Best-fit lines from the modified creep power law equation (Eq. (1)) are given together with the resulting dislocation creep threshold stresses. The colored best-fit curve (dash-dot) represents only the first four data points for the Al-0.06Sc-0.06Zr-0.02Sb at% alloy, while the grey best fit curve (dashed) represents all data points and gives a threshold stress of 7.1 MPa. Creep rates for pure Al are also plotted [66]. (For interpretation of the references to color in this figure legend, the reader is referred to the web version of this article.)

strengthening due to Zr precipitation.

The Vickers microhardness and electrical conductivity measurements for the Al-Sc-Zr-Sb alloy, isothermally aged at 400 and 425 °C after prior peak aging at 300 °C for 4 h, are displayed in Fig. 8. Aging at 400 °C for 24 h yields a peak microhardness value of 640 ± 9 MPa, with a concomitant conductivity of 33.04 ± 0.03 MS/m, which are comparable to the values achieved during isothermal aging at 300 °C for 56 days, Fig. 6. A slightly lower microhardness is achieved after 24 h for aging at 425 °C, which is the result of a smaller driving force for nucleation. The microhardness values at 425 °C decrease significantly after aging for more than a week, while this decrease is less pronounced at 400 °C. These results imply that a total aging time of 12 h (at 300 and then 400 °C) leads to peak alloy strength, which is more than 50 times shorter than the time (64 days) required for aging at only 300 °C.

### 3.4. Creep results at 300 °C

A plot of the steady-state strain rate vs. the applied stress during creep experiment of our Al-0.066Sc-0.050Zr-0.021Sb (at%) alloy at 300 °C is displayed in Fig. 9, along with the data for the Al-0.057Sc-0.059Zr alloy (at%, measured using DCP-OES) studied by Knipling et al. [3]. While the creep specimen from our Sb-containing alloy was aged isochronally to 450 °C utilizing 25 °C/1 h steps, the Sb-free creep specimen was aged isochronally to 400 °C with 25 °C 3 $h^{-1}$ steps. Because Knipling's Al-0.06Sc-0.06Zr (at%) alloy aged isochronally to 400 °C with 25 °C 3 $h^{-1}$ steps has a Vickers microhardness value similar to that of Booth-Morrison et al. Al-0.052Sc-0.067Zr (at%, measured with DCP-OES) alloy aged isochronally to 450 °C with 25 °C/1 h steps, it is likely that the two alloys have similar microstructure and therefore it is reasonable to use Knipling et al.'s creep dataset to compare with our Sb-containing alloy [3,47]. No 300 °C creep data are available for the Al-Sc-Zr alloy studied by Booth-Morrison et al. [52].

The steady-state strain-rate $\dot{\varepsilon}$ vs. applied stress σ data points (Fig. 9) are fitted to the modified power-law equation:

$$\dot{\varepsilon} = A(\sigma - \sigma_{th})^n \exp\left(-\frac{Q}{RT}\right) \quad (1)$$

where $A$ is a constant, $\sigma_{th}$ is the threshold stress below which the steady-state strain-rate cannot be measured in the laboratory frame, $R$ is the ideal gas constant, $T$ is the absolute temperature, $n$ is a creep-mechanism dependent exponent, and $Q$ is the activation energy for self-diffusion [60,66–68]. The activation energy is taken to be $Q$ =142 kJ $mol^{-1}$ for pure aluminum, and the creep exponent can be taken as that of dislocation creep ($n$=4.4), since the micrograph of the creep specimen (Fig. 2) exhibits large grain diameters indicating that diffusional creep is not dominant [61,62]. The constant $A$ and threshold stress $\sigma_{th}$ for the Sb-containing alloys are determined from a nonlinear fit of $\dot{\varepsilon}^{1/n}$ vs. σ, yielding $\sigma_{th}$ =10 MPa when using the four lowest stress data points. Knipling et al. reported $\sigma_{th}$=12 MPa for a creep specimen tested at 300 °C [3], Fig. 9. Further experiments are required to confirm the mechanisms controlling the creep behavior in this alloy, which are beyond the scope of this paper whose focus is precipitate evolution.

For applied stresses below ~15 MPa, the best-fit curves suggest that Knipling et al.'s Sb-free Al-Sc-Zr specimen is somewhat more creep resistant than our Sb-containing alloy. The Al-Sc-Zr data only includes steady-state strain-rates for applied stresses > 13 MPa, and a more appropriate fit of the power law equation would incorporate data for smaller applied stresses. It is, however, clear that our Sb-containing alloy has superior creep resistance for applied stresses > 15 MPa, since the steady-state strain-rates are significantly smaller than those measured on the Al-Sc-Zr alloy by approximately more than one order of magnitude at 20 MPa.

## 4. Discussion

### 4.1. Core-shell precipitate structure

The precipitates present within the Al-Sc-Zr-Sb samples, which were aged isochronally to 450 °C, display a similar morphology to those of the Sb-free alloy [3,40,47–50]: Sc-rich core and Zr-rich shell. The proxigrams generated from the precipitates within the atom-probe tomographic nanotip for the Al-Sc-Zr-Sb alloy (Fig. 5) indicate that Sb is present throughout the precipitates, but clearly segregates to the Zr-shell of the precipitates where there is a peak concentration of 0.4 at% of Sb, a value twenty times greater than the nominal nanotip concentration of 0.02 at% Sb. Additionally, the Sb appears to be enriched wherever there is a significant concentration of Zr ( > 1 at %). We hypothesize that a favorable attractive binding energy between Zr and Sb together with a favorable attractive binding energy of 0.30 eV [55] between Sb and vacancies accelerates the diffusion kinetics of Zr in Al, and thus the growth kinetics of the Zr-rich shell, but first-principle calculations need to be performed to confirm this model. While Wolverton et al. 7/1/16 11:35 p.m. calculate a repulsive binding energy between Zr and vacancies at first nearest- neighbors to be ~0.28 eV, it is possible that the Zr-Sb-vacancy trimers are energetically favorable. The Sb-Zr binary phase diagram indicates the existence of several equilibrium intermetallic compounds on the Zr-rich side, which support the idea that there is a favorable attractive binding energy between Zr and Sb. Zirconium precipitation in the Sb-free alloy is hampered by the formation of Zr-rich primary precipitates that form during solidification or homogenization and by segregation at the dendrites during solidification; the ability of Sb to promote incorporation of Zr into the precipitates is a desirable result [3,38,69]. Based on the data from isochronal and isothermal aging at 300 °C (Fig. 3), Sb does not appear to have any detectable effect on the formation kinetics of the Sc-rich precipitate cores, unlike Er and Si [47,53]. No Sc-Sb phase diagram exists in the literature, and it is unknown whether or not Sc and Sb atoms display attractive binding energies.

### 4.2. Precipitation kinetics

The Vickers microhardness and electrical conductivity measurements as a function of aging temperature during isochronal aging (Fig. 3) provide an indirect way to follow the evolution of the $Al_3(Sc, Zr)$ precipitates in the alloy. Generally, for aging at low temperatures, increases in microhardness and electrical conductivity values correspond to nucleation and growth of the precipitates, which both improve an alloy's ability to resist plastic deformation and deplete the α-Al matrix of solute atoms as the volume fraction of precipitates increases [3,5,64]; solute atoms disrupt the three three-dimensional periodicity of the lattice and hence have a large cross-section for scattering electrons. For aging at high temperatures, a decrease in microhardness values corresponds to precipitate coarsening and the transition from particle shearing to Orowan dislocation looping, a phenomenon previously established in Refs. [3,22,27,38,43,47,54,60,64,70], while dissolution of the precipitates begins when the electrical conductivity starts to decrease as a result of electron-scattering by solute atoms dissolving in the matrix.

Samples aged isochronally tend to display a larger number density of precipitates as they are formed at the lowest possible temperature with a high driving-force for nucleation. The Al-Sc-Zr-Sb alloy has ~50 MPa higher microhardness values than the Al-Sc-Zr alloy for isochronal aging temperatures between 100 and 275 °C (Fig. 3), which may be the result of the formation of extremely fine Sb-rich nano-precipitates in the Sb-containing alloy during homogenization. Future LEAP tomography will need to be performed on as-homogenized samples to verify the existence of Sb-rich precipitates. These precipitates, if they exist, may act as heterogeneities for the nucleation of $Al_3(Sc, Zr)$ precipitates created subsequently at higher temperatures, and may explain why Sb is found, albeit in small quantities, in the cores of the precipitates (Fig. 5).

LEAP tomographic data on the Al-Sc-Zr-Sb sample aged isochronally to 450 °C (Fig. 4) indicate that there is a larger number density and volume fraction of precipitates compared to Al-Sc-Zr employing the same aging condition, suggesting that the accelerated precipitation kinetics is driven by an increase in the nucleation rate caused by Sb. Although no LEAP tomographic data for an alloy aged isothermally at 400 °C exist, it is likely that the Sb-containing alloy forms a much higher number density and volume fraction of precipitates than the Al-Sc-Zr alloy, based on the ~240 MPa discrepancy in microhardness values. Because Sb has an attractive nearest-neighbor binding energy of ~0.30 eV with vacancies in Al (higher than for Si), for which the attractive binding energy is ~0.03 eV [55]. The resulting vacancy clusters may act as heterogeneous nucleation sites for precipitates, which would explain the larger number density of precipitates in Al-Sc-Zr-Sb [55].

The nucleation current (number of nuclei formed per unit time per unit volume) is determined by the net reversible work, $W_R$, required to make a nucleus (precipitate) of radius R [66,71]. Classical nucleation theory states that the supersaturation of an element in an alloy depends on a Helmholtz free energy expression, which has both a chemical energy component, $\Delta F_{ch}$ (which is negative), and an elastic strain energy component, $\Delta F_{el}$ (which is always positive). The Helmholtz free energy expression also contains an interfacial free energy term, $\sigma^{\alpha/\beta}$, which is always positive. The net reversible work required for the formation of a spherical nucleus, $W_R$, as a function of the nucleus' radius, $R$, is given by:

$$W_R=(\Delta F_{ch}+\Delta F_{el})\frac{4\pi}{3}R^3+4\pi R^2\sigma^{\alpha/\beta} \tag{2}$$

The critical radius, $R^*$, for nucleation is given by:

$$R^*=-\frac{2\sigma^{\alpha/\beta}}{\Delta F_{ch}+\Delta F_{el}} \tag{3}$$

and the critical net reversible work required for the formation of a critical spherical nucleus, $W_R^*$, is given by:

$$W_R^*=\frac{16\pi}{3k_BT}\frac{(\sigma^{\alpha/\beta})^3}{(\Delta F_{ch}+\Delta F_{el})^2} \tag{4}$$

The nucleation current is proportional to:

$$\exp\left(-\frac{16\pi}{3k_BT}\frac{(\sigma^{\alpha/\beta})^3}{(\Delta F_{ch}+\Delta F_{el})^2}\right) \tag{5}$$

where $k_B$ is Boltzmann's constant and T is the absolute temperature. Therefore, the nucleation current is very sensitive to the cube of the interfacial free energy and square of the sum of the chemical and elastic free energy terms.

Segregation of Sb at the matrix/nucleus interface decreases the interfacial free energy as demanded by the Gibbs adsorption isotherm, which concomitantly increases the nucleation current [66,72]. First-principles calculations need to be performed to obtain the magnitude of the effect of Sb on the matrix/nucleus (precipitate) interfacial free energy.

Our Al-Sc-Zr-Sb alloy has a consistently higher microhardness compared to Al-Sc-Zr during isochronal aging between 475 and 575 °C (Fig. 3), which indicates a slower coarsening and dissolution rate of the Sb-containing precipitates. The Lifshitz-Slyozov-Wagner (LSW) model indicates that the diffusion-limited coarsening rate of nuclei (precipitates) is proportional to the diffusivity of the slowest moving solute species and the matrix/nucleus (precipitate) interfacial free energy [15]. One possible explanation for the seemingly contradictory combination of faster precipitation kinetics and slower coarsening kinetics is that Sb acts via two separate mechanisms depending on its location: (i) in solid-solution in the Al-matrix, Sb may increase the diffusivity of Zr by decreasing the migration energy of Zr in Al due

to an attractive binding energy between Sb atoms and vacancies, similar to the effects of Si on increasing scandium's diffusivity [53], resulting in faster nucleation kinetics and growth kinetics of the Zr-rich regions of the precipitate; (ii) Sb atoms segregating at the matrix/precipitate decrease its interfacial free energy, which concomitantly decreases the coarsening rate. A careful combined experimental and modeling study, which is beyond the scope of the present article, is needed to test this hypothesis.

### 4.3. Strengthening mechanisms at ambient temperature

The equations for the four precipitation strengthening mechanisms anticipated for the Al-Sc-Zr system are given in the Appendix A: (i) modulus; (ii) coherency; (iii) order, and (iv) Orowan dislocation looping [27,39,60,64]. The first three mechanisms are observed for shearable precipitates, while Orowan dislocation looping is observed for unshearable precipitates [27,43,60,68]. Our Al-Sc-Zr-Sb alloy has an approximately 50 MPa higher microhardness than does Al-Sc-Zr for isochronal aging temperatures between 100 and 275 °C, which is unlikely due to solid-solution strengthening because the difference in solute atom concentrations between the Sb-free and Sb-containing alloys is only 200 at. ppm, Table 4. The difference in microhardness between the two alloys at low isochronal aging temperatures may be the result of the formation of Sb-rich nanoscale precipitates, although we need additional atom-probe tomography experiments to confirm this.

The contribution of each mechanism is displayed in Table 4 for the Sb-free and Sb-containing alloys isochronally aged to 450 °C. Prior studies on the Al-Sc-Zr system have demonstrated that the critical mean radius for the transition from shearable to unshearable precipitates is ~2–3 nm, and a similar trend is anticipated for Al-Sc-Zr-Sb [3,43].

Following Refs. [60,68,73] the total increase in an alloy's yield strength due to aging is obtained by subtracting the homogenized state's microhardness after aging, and dividing it by three. Coherency, modulus, and order strengthening mechanisms operate in sequence and the dominant mechanism is the one that has the highest calculated yield strength increment; in this case the coherency and modulus strengthening are the dominant mechanisms. Since the Orowan dislocation looping and shearing mechanisms operate in parallel, the one with smaller strengthening contribution is dominant. Thus, as shown in Table 4, coherency/modulus strengthening and Orowan dislocation looping dictate the strengthening of the alloy for average precipitate radii below and above the critical transitional radii, respectively. The discrepancy between our observations and the calculations may be the result of an inhomogeneous distribution of precipitates due to the dendritic structure; Zr is concentrated in the dendrites and depleted in it between them, which leads to deleterious effects on the overall alloy strength [5,38]. It is also possible that the measured volume fraction of the precipitates from the LEAP tomographic nanotip is greater than the overall alloy volume fraction, since the tip may have been taken from a region that is solute-enriched due to segregation.

After two months of aging at 300 °C, the Sb-containing alloy displays a microhardness that is ~80 MPa higher than the Sb-free alloy (corresponding to an increase in yield strength of ~27 MPa), which may be the result of the formation of a Zr-rich shell at much earlier aging times for the Sb-containing alloy. The formation of the Zr-rich shell creates regions within the precipitate with the ordered $L1_2$ $Al_3Zr$ structure, which adds to the order strengthening contribution. Similarly, the ~80 MPa yield strength discrepancy between the Sb-free and Sb-containing alloy after aging at 400 °C for 4 h is because of the higher number density and volume fraction of precipitates in the latter caused by a larger nucleation current.

**Table 4**
Experimental yield strength increments, and calculated yield strength increments for four different mechanisms: (1) modulus strengthening $\Delta\sigma_{ms}$ (Eq. (1)); (2) coherency strengthening $\Delta\sigma_{ms}$ (Eq. (2)); (3) order strengthening $\Delta\sigma_{os}$ (Eq. (3)); and Orowan dislocation looping, $\Delta\sigma_{or}$ (Eq. (4)). The values are reported for the Sb-free[21] and Sb-containing alloys after homogenization at 640 °C for 72 h and isochronal aging through 450 °C with a heating rate of 8 K $h^{-1}$.

| Alloy | ΔHV/3 (MPa) | $\Delta\sigma_{os}$ (MPa) | $\Delta\sigma_{cs}+\Delta\sigma_{ms}$ (MPa) | $\Delta\sigma_{or}$ (MPa) |
|---|---|---|---|---|
| Al-Sc-Zr[21] | 132 ± 4 | 118 ± 1 | 165 ± 5 | 112 ± 20 |
| Al-Sc-Zr-Sb | 123 ± 5 | 197 ± 2 | 319 ± 32 | 206 ± 20 |

### 4.4. Creep resistance

The creep behavior of the Al-0.066Sc-0.050Zr-0.021Sb at% specimen aged isochronally to 450 °C with 25 °C/1 h steps (corresponding to the highest hardness, Fig. 3) is compared to an Sb-free alloy with similar Sc and Zr composition (Al-0.067Sc-0.052Zr at%) specimen aged isochronally to 400 °C with 25 °C/3 h steps [3]. While the Sb-containing alloy has a threshold stress (~10 MPa) similar to that of the Sb-free alloy (~12 MPa) at 300 °C, the former exhibits a significantly lower steady-state strain-rates for applied compression stresses above ~15 MPa. The improvement in creep resistance from Sb microalloying may be the result of the following: (i) increased lattice parameter mismatch between the precipitates and the matrix as a result of Sb segregation to the Zr-rich shell of the precipitates, leading to an increased elastic interaction between the precipitates and dislocations [67]; and/or (ii) accelerated formation of a Zr-rich precipitate shell during creep at 300 °C, which leads to coarser $Al_3$(Sc, Zr) precipitates that exhibit greater resistance to dislocation shearing and climbing [60,66]. Without in situ observations of precipitate-dislocation interactions via TEM and/or computational dislocation dynamics simulations for the Sb-containing alloy during creep at 300 °C, we are only able to propose some possible mechanisms responsible for the different observed creep behavior. Further experiments are necessary to confirm the actual mechanisms controlling creep, which are beyond the scope of this paper whose focus is on precipitate evolution.

Alloys with trialuminide-forming rare-earth elements (e.g., Yb, Er, and Gd) have yielded improvements in creep resistance, while those with transition elements (e.g. Ti, Zr) and Li and Mg reduce creep resistance [33,34,52,70,74–79]. Van Dalen et al. [78,80] studied Al-Sc alloys with Yb and Gd additions and found that the greater the matrix-precipitate lattice parameter mismatch resulting from these rare-earth elements partitioning to the precipitates lead to superior creep resistance as a result of increased elastic interactions between the precipitates and dislocations. The same conclusion was reached by Booth-Morrison et al. [52] who studied Al-Sc-Zr-Si alloys with Er additions. Alternatively, Krug et al. [81,82] studied the effects of Li on Al-Sc alloys and found that the resulting decreased lattice parameter mismatch due to the replacement of Sc by Li on the Sc sublattice of the $L1_2$ structure leads to a lower threshold stresses; they found a similar trend for alloys with transition elements such as Zr and Ti.

In the present alloys, Sb additions appear to have less of an effect on creep resistance than rare-earth elements, since Sb additions do not produce a significant change in the threshold stress (~10 MPa) as compared with rare-earth elements (~20–23 MPa for Yb). Antimony additions have, however, the effect of improving the coarsening resistance of the precipitates at elevated temperatures, which may help maintain the alloy's creep resistance. This opens the door to further improving the creep resistance of an Al-Sc-Zr-Sb alloy with rare-earth additions by increasing the lattice parameter mismatch; however, additional studies are necessary to ensure that the rare-earth additions do not hinder the incorporation of Sb into the $Al_3$(Sc, Zr) precipitates.

## 5. Conclusions

The effects of Sb micro-additions to a dilute Al-Sc-Zr alloy upon the

$Al_3$(Sc, Zr) precipitate composition and growth and coarsening kinetics have been studied in a Al-0.066Sc-0.050Zr-0.021Sb at% alloy by Vickers microhardness and electrical conductivity measurements, and LEAP tomographic three-dimensional reconstructions, for alloys aged for different times and temperatures during isochronal and isothermal aging experiments. The following conclusions are reached concerning the effect of Sb additions to dilute Al-Sc-Zr alloys:

1. Antimony accelerates the formation kinetics of the Zr-rich precipitate shell, as compared to a control Sb-free alloy. This is supported by: (i) a lack of microhardness decrease during isochronal aging between 350 and 450 °C; (ii) an increase in microhardness following two weeks of isothermal aging at 300 ° (iii) achievement of increased microhardness values when aged isothermally at 400 °C (~450 MPa in the Sb-containing and ~230 MPa in the Sb-free alloy). The faster kinetics of Zr precipitation may be due to an attractive interaction between Sb and Zr atoms, and/or attraction between Sb and vacancies, which leads to a formation of vacancy clusters that serve as heterogeneous nucleation sites for Zr precipitation.
2. Antimony is incorporated within the $Al_3$(Sc, Zr) precipitates and is enriched where Zr atoms are present. LEAP tomographic observations demonstrate that Sb atoms in the Zr-rich shell of the precipitates achieve concentrations as high as 0.35 at%. This is consistent with the above hypothesis of an attractive Sb-Zr interaction.
3. Antimony improves the coarsening resistance of the alloy, leading to a decrease in the microhardness and conductivity, during isochronal aging, which is more sluggish than in the control Sb-free alloy. This may be the result of Sb decreasing the interfacial free energy of the matrix/precipitate interface.
4. Antimony improves the creep resistance of the alloy for compressive stresses above ~15 MPa at 300 °C. This may originate from an increased precipitate-matrix lattice mismatch due to the Sb presence in the precipitates, and/or further growth of the Zr- and Sb-rich precipitate shell during creep testing. However, more experiments beyond the scope of this paper are needed to confirm the creep mechanisms.

## Acknowledgements

Dr. Nhon Q. Vo (NanoAl LLC) is acknowledged for providing guidance in performing heat-treatment and creep experiments. Research Professor Dieter Isheim of the Northwestern University Center for Atom-Probe Tomography (NUCAPT) is recognized for assistance and training in performing LEAP tomographic experiments. The LEAP tomography system was purchased and upgraded with funding from NSF-MRI (DMR-0420532) and ONR-DURIP (N00014-0400798, N00014-0610539 and N00014-0910781) grants. The authors also gratefully acknowledge the Initiative for Sustainability and Energy at Northwestern (ISEN) for grants to upgrade the capabilities of NUCAPT. Finally, we thank Dr. Carla Shute of the Northwestern University Optical Microscopy and Metallography (OMM) Laboratory for many helpful discussions and assistance in using equipment in the OMM facility, which receives support from the MRSEC Program (NSF DMR-1121262) of the Materials Research Center at Northwestern University.

## Appendix A

Following Refs. [3,5,21,27,43,47,54,83], we describe herein briefly the equations used to calculate theoretical strengthening contributions from both shearable and unshearable precipitates.

Modulus strengthening, $\Delta\sigma_{ms}$, arises from the mismatch in shear moduli between the $Al_3$(Sc,Zr) precipitates and the α-Al matrix; the contribution from this mechanism is calculated from the following equation:

$$\Delta\sigma_{ms} = M0.0055(\Delta G)^{3/2}\left(\frac{2f}{Gb^2}\right)^{1/2} b\left(\frac{\langle r\rangle}{b}\right)^{(3m/2)-1} \quad \text{(A1)}$$

where $M$=3.06 is the matrix orientation factor, $G_m$ is the shear modulus of Al, ΔG is the mismatch of moduli between the precipitate and the matrix ($G_p$–$G_m$), $b$ is the magnitude of aluminum's Burgers vector, $m$=0.85 is a constant, and $f$ is the volume fraction of the precipitates [11,43,60,64]. The matrix modulus is taken as $G_m$=25.4 GPa, $G_p$=68 GPa assuming that $Al_3$(Sc,Zr) and $Al_3$Sc precipitates have the same shear moduli, and $b$ =0.286 nm for pure Al [11,27,43,60,64].

Coherency strengthening, $\Delta\sigma_{cs}$, comes from the interaction between the strain fields of the mismatched lattice parameters of the matrix and precipitate, and dislocations [60,64,68]. Eq. (A2) models this strengthening mechanism [27,43]:

$$\Delta\sigma_{cs} = M\chi(\varepsilon G)^{3/2}\left(\frac{\langle r\rangle f}{0.18Gb}\right)^{1/2} \quad \text{(A2)}$$

The lattice parameter misfit term ε is equal to $(2/3)\delta$ where $\delta=(a_p-a_m)/a_m$, and $a_p$ and $a_m$ are the lattice parameters for the precipitate and matrix, respectively [11,27,43,60,68]. The lattice parameter of the matrix from literature is 4.050 Å, while the lattice parameter of the precipitate is 4.103 Å, taken as that of $Al_3$Sc [1]. Finally, the χ=2.6 term is taken to be a constant [43,64].

Order strengthening, $\Delta\sigma_{os}$, occurs when a dislocation shears an ordered intermetallic-precipitate, disrupting the favorable bonding of the ordered atomic arrangement within the secondary phase [60,64,68]. The resistance to precipitate shearing by this mechanism is modeled by using following equation [27,43,60,64,68]:

$$\Delta\sigma_{os} = M0.81\frac{\gamma_{apb}}{2b}\left(\frac{3\pi f}{8}\right)^{1/2} \quad \text{(A3)}$$

The energy penalty for creating an antiphase boundary by disrupting low-energy state arrangements of atoms within the precipitate manifests itself in an antiphase boundary interfacial energy, $\gamma_{apb}$, term [60,64]. This mechanism is prevalent in nickel-based superalloys strengthened by ordered and coherent γ′($L1_2$)-precipitates, and thus resistance to antiphase boundary formation is expected to provide significant strengthening in Al-Sc-Zr alloys.

Orowan strengthening, $\Delta\sigma_{or}$, by dislocation bowing around precipitates occurs when the precipitate becomes too big or too strong to be sheared [60,64,68]. This strengthening mechanism is modeled by the following equation [27,43,60,64,68]:

$$\Delta\sigma_{or} = M\frac{0.4Gb}{\pi\lambda}\frac{\ln(2\bar{r}/b)}{\sqrt{1-\nu}} \tag{A4}$$

Poisson's ratio ν for aluminum is 0.345, the mean radius of a circular cross-section in a random plane for a spherical precipitate is given by $\bar{r} = \sqrt{2/3}\langle r\rangle$, and the inter-precipitate spacing, λ, is given by the following equation [12,16,43,64,84]:

$$\lambda = 2\bar{r}\left(\sqrt{\frac{\pi}{4f}} - 1\right) \tag{A5}$$

## References


[1] K.E. Knipling, D.C. Dunand, D.N. Seidman, Criteria for developing castable, creep-resistant aluminum-based alloys – a review, Z. Metall. 97 (2006) 246–265.
[2] K.E. Knipling, Development of a Nanoscale Precipitation-Strengthened Creep-Resistant Aluminum Alloy Containing Trialuminide Precipitates, Northwestern University, Evanston, IL, 2006.
[3] K.E. Knipling, D.N. Seidman, D.C. Dunand, Ambient- and high- temperature mechanical properties of isochronally aged Al-0.06Sc, Al-0.06 Zr, and Al-0.06Sc-0.06Zr alloys (at%), Acta Mater. 59 (2011) 943–954.
[4] V.V. Zakharov, Combined alloying of aluminum alloys with scandium and zirconium, Metal Sci. Heat Treat. 56 (2014) 281–286.
[5] K.E. Knipling, R.A. Karnesky, C.P. Lee, D.C. Dunand, D.N. Seidman, Precipitation evolution in Al–0.1Sc, Al–0.1Zr and Al–0.1Sc–0.1Zr (at%) alloys during isochronal aging, Acta Mater. 58 (2010) 5184–5195.
[6] C.B. Fuller, A.R. Krause, D.C. Dunand, D.N. Seidman, Microstructure and mechanical properties of a 5754 aluminum alloy modified by Sc and Zr additions, Mater. Sci. Eng. A 338 (2002) 8–16.
[7] C.B. Fuller, D.N. Seidman, D.C. Dunand, Structure-property relationships for Al(Sc, Zr) alloys, in: Hot Deformation of Aluminum Alloys III, TMS Warrendale, PA, 2003, pp. 531–540
[8] J.Z. Dang, Y.F. Huang, J. Cheng, Effects of Sc and Zr on microstructures and mechanical properties of as-cast Al-Mg-Si-Mn alloys, Trans. Nonferrous Met. Soc. China 19 (2009) 540–544.
[9] Y.D. He, X.M. Zhang, Z.Q. Cao, Effects of minor Sc and Zr addition o grain refinement of as-cast Al-Zn-Mg-Cu alloys, China Foundry 6 (2009) 214–218.
[10] Z. Jia, J. Røyset, J.K. Solberg, Q. Liu, Formation of precipitates and recrystallization resistance in Al–Sc–Zr alloys, Trans. Nonferrous Met. Soc. China 22 (2012) 1866–1871.
[11] A.K. Vasudevan, R.D. Doherty, Aluminum Alloys–Contemporary Research and Applications: Contemporary Research and Applications, Elsevier, USA, 2012.
[12] R.J. Hussey, J. Wilson, Light Alloys: Directory and Databook, Springer Science & Business Media, 2013.
[13] Accelerated Aging of Materials and Structures: The effects of long-term elevated-temperature exposure, National Academy Press, Washington D.C, 1996
[14] J.E. Hatch, Aluminum: properties and metallurgy, Am. Soc. Met. (1984).
[15] L. Ratke, P.W. Voorhees, Growth and Coarsening: Ripening in Material Processing, Springer-Verlag, Germany, 2002.
[16] Metals Handbook, vol. 2 – Properties and Selection: Nonferrous Alloys and Special-Purpose Materials, 10th ed., ASM International, 1990
[17] J. Royset, N. Ryum, Scandium in aluminum, Int. Mater. Rev. 50 (2005).
[18] E.A. Marquis, D.N. Seidman, Nanoscale structural evolution of Al3Sc precipitates in Al(Sc) alloys, Acta Mater. 49 (2001) 1909–1919.
[19] K.E. Knipling, D.C. Dunand, D.N. Seidman, Precipitation evolution in Al-Zr and Al-Zr-Ti alloys during aging at 450–600 °C, Acta Mater. 56 (2008) 1182–1195.
[20] S.-I. Fujikawa, Impurity diffusion of scandium in aluminium, Defect Diffus. Forum 143–147 (1997) 115–120.
[21] K.E. Knipling, D.C. Dunand, D.N. Seidman, Nucleation and precipitation strengthening in dilute Al-Ti and Al-Zr alloys, Metall. Mater. Trans. A 38 (2007) 2552–2563.
[22] E.A. Marquis, D.N. Seidman, Coarsening kinetics of nanoscale Al3Sc precipitates in an Al-Mg-Sc alloy, Acta Mater. 53 (2005) 4259–4268.
[23] T. Torma, E. Kovács-Csetényi, T. Turmezey, T. Ungár, I. Kovács, Hardening mechanisms in Al-Sc alloys, J. Mater. Sci. 24 (1989) 3924–3927.
[24] H.-H. Jo, S.-I. Fujikawa, Kinetics of precipitation in Al3Sc alloys and low temperature solid solubility of scandium in aluminium studied by electrical resistivity measurements, Mater. Sci. Eng.: A 171 (1993) 151–161.
[25] S. Iwamura, Y. Miura, Loss in coherency and coarsening behavior of Al3Sc precipitates, Acta Mater. 52 (2004) 591–600.
[26] G.M. Novotny, A.J. Ardell, Precipitation of Al3Sc in binary Al–Sc alloys, Mater. Sci. Eng.: A 318 (2001) 144–154.
[27] E.A. Marquis, D.N. Seidman, D.C. Dunand, Precipitation strengthening at ambient and elevated temperatures of heat-treatable Al(Sc) alloys, Acta Mater. 51 (2003) 285–287.
[28] K. Hirano, S. Fujikawa, Impurity diffusion in aluminum, J. Nucl. Mater. 69–70 (1978) 564–566.
[29] E. Nes, Precipitation of the metastable cubic Al3Zr-phase in subperitectic Al-Zr alloys, Acta Metall. 20 (1972) 499–506.
[30] R.W. Hyland, Homogeneous nucleation kinetics of Al3Sc in a dilute Al-Sc alloy, Metall. Trans. A 23 (1992) 1947–1955.
[31] E.A. Marquis, D.N. Seidman, D.C. Dunand, Creep of precipitation-strengthened Al(Sc) alloys, in: Creep Deformation: Fundamentals and Applications, TMS Warrendale, PA, 2002, pp. 299–308
[32] B. Smola, I. Stulíková, V. Očenášek, J. Pelcová, V. Neubert, Annealing effects in Al–Sc alloys, Mater. Sci. Eng.: A 462 (2007) 370–374.
[33] M.E. van Dalen, D.N. Seidman, D.C. Dunand, Creep and coarsening properties of Al-0.06 at% Sc-0.06 at% Ti at 300–450 °C, Acta Mater. 56 (2008) 4369–4377.
[34] E.A. Marquis, D.N. Seidman, D.C. Dunand, Microstructural, and creep properties of an Al-2 Mg-0.2 Sc (wt%) alloy, in: Hot Deformation of Aluminum Alloys III, TMS Warrendale, PA, 2003, pp. 177–184
[35] M. Alatalo, M. Weinert, R.E. Watson, Stability of Zr-Al alloys, Phys. Rev. 57 (1998).
[36] T. Ohashi, R. Ichikawa, A new metastable phase in rapidly solidified Al-Zr alloys, Metall. Trans. 3 (1972) 2300–2302.
[37] T. Gao, X.L. Cui, X.Y. Li, H. Li, X.F. Liu, Morphological evolutions and growth patterns of Zr-containing phases in aluminum alloys, CrystEngComm 16 (2014) 3548–3557.
[38] K.E. Knipling, D.C. Dunand, D.N. Seidman, Precipitation evolution in Al–Zr and Al–Zr–Ti alloys during isothermal aging at 375–425 °C, Acta Mater. 56 (2008) 114–127.
[39] C.B. Fuller, Temporal Evolution of the Microstructures of Al(Sc,Zr) Alloys and Their Influences on Mechanical Properties, 2003
[40] W. Lefebvre, F. Danoix, B. Forbord, 3D atom probe investigation of precipitation in the Al-Sc-Zr system, in: Solid-Solid Phase Transformations in Inorganic Material, Minerals, Metals & Materials Society, Phoenix, AZ, 2005, pp. 511–516
[41] A. Tolley, V. Radmilovic, U. Dahmen, Coarsening kinetics in Al-Sc-Zr alloys, in: Solid-Solid Phase Transformations in Inorganic Material, Minerals, Metals & Materials Society, Phoenix, AZ, 2005, pp. 785–790
[42] M. Song, Y. He, S. Fang, Effects of Zr content on the yield strength of an Al-Sc alloy, J. Mater. Eng. Perform. 20 (2011) 377–381.
[43] C.B. Fuller, D.N. Seidman, D.C. Dunand, Mechanical properties of Al(Sc,Zr) alloys at ambient and elevated temperatures, Acta Mater. 51 (2003) 4803–4814. http://dx.doi.org/10.1016/S1359-6454(03)00320-3.
[44] N.A. Belov, A.N. Alabin, D.G. Eskin, V.V. Istomin-Kastrovskii, Optimization of hardening of Al-Zr-Sc cast alloys, J. Mater. Sci. 41 (2006) 5890–5899.
[45] H. Zapolsky, J. Boisse, R. Patte, N. Lecoq, Phase field simulation of coarsening kinetics in Al-Sc and Al-Sc-Zr alloys, in: Advanced Intermetallic-Based Alloys for Extreme Environment and Energy Applications, Materials Research Society, 2009, pp. 549–554
[46] C.B. Fuller, D.N. Seidman, Temporal evolution of the nanostructure of Al(Sc,Zr) alloys: part II—coarsening of Al3Sc1-xZrx precipitates, Acta Mater. 53 (2005) 5415–5428.
[47] C. Booth-Morrison, D.C. Dunand, D.N. Seidman, Coarsening resistance at 400 °C of precipitation strengthened Al-Zr-Sc-Er alloys, Acta Mater. 59 (2011) 7029–7042.
[48] A. Tolley, V. Radmilovic, U. Dahmen, Segregation in Al-3(Sc,Zr) precipitates in Al-Sc-Zr alloys, Scr. Mater. 52 (2005) 621–625.
[49] A.K. Lohar, B. Mondal, D. Rafaja, V. Klemm, S.C. Panigrahi, Microstructural investigations on as-cast and annealed Al-Sc and Al-Sc-Zr alloys, Mater. Charact. 60 (2009) 1387–1394.
[50] E. Clouet, M. Nastar, A. Barbu, C. Sigli, G. Martin, An atomic and mesoscopic study of precipitation kinetics in Al-Zr-Sc alloys, Adv. Eng. Mater. 8 (2006) 1228–1231.
[51] C. Monachon, D.C. Dunand, D.N. Seidman, Atomic-scale characterization of aluminum-based multishell nanoparticles created by solid-state synthesis, Small 6 (2010) 1728–1731.
[52] C. Booth-Morrison, D.N. Seidman, D.C. Dunand, Effect of Er additions on ambient and high-temperature strength of precipitation-strengthened Al-Zr-Sc-Si alloys, Acta Mater. 60 (2012) 3643–3654. http://dx.doi.org/10.1016/j.actamat.2012.02.030.
[53] Z.M.C. Booth-Morrison, Role of silicon in accelerating the nucleation of Al3(Sc,Zr) precipitates in dilute Al-Zr-Sc alloys, Acta Mater. 60 (2012).
[54] N.Q. Vo, D.C. Dunand, D.N. Seidman, Improving aging and creep resistance in a dilute Al–Sc alloy by microalloying with Si, Zr and Er, Acta Mater. 63 (2014) 73–85.
[55] C. Wolverton, Solute–vacancy binding in aluminum, Acta Mater. 55 (2007) 5867–5872.
[56] H. Okamoto, The Sb-Zr (antimony-zirconium) system, JPE 14 (1993) 228–231. http://dx.doi.org/10.1007/BF02667815.
[57] A.J. McAlister, The Al-Sb (aluminum-antimony) system, Bull. Alloy Phase Diagr. 5 (1984) 462–465.
[58] H. Okamoto, Al-Sb (aluminum-antimony), J. Phase Equilibria 18 (1997).
[59] R. Balakumar, M. Medraj, Thermodynamic Modeling of the Mg-Al-Sb System 29, Elsevier, Montreal, CA, 2005, pp. 24–36.
[60] T.H. Courtney, Mechanical Behavior of Materials, McGraw Hill, Long Grove, IL, 2000.

[61] H.J. Frost, M.F. Ashby, Deformation-Mechanism Maps, The Plasticity and Creep of Metals and Ceramics, 1st ed., Pergamon Press, USA, 1982.
[62] F.A. Mohamed, T.G. Langdon, Deformation mechanism maps based on grain size, Metall. Trans. 5 (1974) 2339–2345.
[63] O.C. Hellman, J.A. Vandenbroucke, J. Rüsing, D. Isheim, D.N. Seidman, Analysis of three-dimensional atom-probe data by the proximity histogram, Microsc. Microanal. 6 (2000) 437–444. http://dx.doi.org/10.1017/S1431927600000635.
[64] A.J. Ardell, Precipitation hardening, Metall. Trans. A 16 (1985) 2131–2165.
[65] D.A. Porter, K.E. Easterling, Phase Transformations in Metals and Alloys, Third ed., CRC Press, USA, 1992 (Revised Reprint).
[66] E.A. Marquis, D.C. Dunand, Model for creep threshold stress in precipitation-strengthened alloys with coherent particles, Scr. Mater. 47 (2002) 503–508.
[67] M.E. Krug, D.C. Dunand, Modeling the creep threshold stress due to climb of a dislocation in the stress field of a misfitting precipitate, Acta Mater. 59 (2011) 5125–5134.
[68] R.W. Hertzberg, Deformation and Fracture Mechanics of Engineering Materials, John Wiley & Sons Canada, Limited, USA, 1983.
[69] H. Okamoto, Sb-Zr (Antimony-Zirconium), 2nd ed., Columbus, OH, 1990.
[70] M. Krug, D. Seidman, D. Dunand, Microstructure and mechanical properties of age-hardening Al-Li-Sc-Yb, Al-Li-Sc, and Al-Sc alloys, Miner. Met. Mater. Soc/AIME (2010) 420 Commonwealth Dr., P. O. Box 430, Warrendale, PA 15086, USA.
[71] Classical Nucleation Theory in Multicomponent Systems, n.d.
[72] M. Hillert, O. Hunderi, N. Ryum, T.O. Sætre, A comment on the Lifshitz-Slyozov-Wagner (L-S-W) theory of particle coarsening, Scr. Metall. 23 (1989) 1979–1981.
[73] P. Zhang, S.X. Li, Z.F. Zhang, General relationship between strength and hardness, Mater. Sci. Eng. A 529 (2011) 62–73.
[74] M. Krug, D. Seidman, D. Dunand, Creep deformation of Al-Sc-X Alloys, Miner. Met. Mater. Soc./AIME (2011) 420 Commonwealth Dr., P. O. Box 430, Warrendale, PA 15086, United States.
[75] Y. Harada, D.C. Dunand, Creep properties of Al3Sc and Al3(Sc, X) intermetallics, Acta Mater. 48 (2000) 3477–3487.
[76] E.A. Marquis, D.C. Dunand, D.N. Seidman, Effect of Mg Addition on the creep and yield behavior of an Al-Sc Alloy, Acta Mater. 51 (2003) 4751–4760.
[77] Y. Harada, D.C. Dunand, Microstructure and creep properties of Al3Sc with ternary transition metal additions, in: Proceedings of the 7th International Conference on Creep and Fatigue at Elevated Temperature (Creep VII), Japan Society of Mechanical Engineers, 2001, pp. 219–226
[78] M.E. van Dalen, T. Gyger, D.C. Dunand, D.N. Seidman, Effects of Yb and Zr microalloying additions on the microstructure and mechanical properties of dilute Al–Sc alloys, Acta Mater. 59 (2011) 7615–7626. http://dx.doi.org/10.1016/j.actamat.2011.09.019.
[79] M.E. van Dalen, D.C. Dunand, D.N. Seidman, Effects of Ti additions on the nanostructure and creep properties of precipitation-strengthened Al-Sc alloys, Acta Mater. 53 (2005) 4225–4235.
[80] M.E. Van Dalen, D.C. Dunand, D.N. Seidman, Microstructural evolution and creep properties of precipitation-strengthened Al–0.06Sc–0.02Gd and Al–0.06Sc–0.02Yb (at%) alloys, Acta Mater. 59 (2011) 5224–5237. http://dx.doi.org/10.1016/j.actamat.2011.04.059.
[81] M.E. Krug, D.N. Seidman, D.C. Dunand, Creep properties and precipitate evolution in Al–Li alloys microalloyed with Sc and Yb, Mater. Sci. Eng.: A 550 (2012) 300–311. http://dx.doi.org/10.1016/j.msea.2012.04.075.
[82] M.E. Krug, D.C. Dunand, D.N. Seidman, Effects of Li additions on precipitation-strengthened Al–Sc and Al–Sc–Yb alloys, Acta Mater. 59 (2011) 1700–1715. http://dx.doi.org/10.1016/j.actamat.2010.11.037.
[83] M.E. van Dalen, D.C. Dunand, D.N. Seidman, Precipitation strengthening in Al (Sc, Ti) alloys, in: Affordable Metal-Matrix Composites for High Performance Applications II, TMS, Chicago, 2003, pp. 195–201
[84] M. Meyers, Mechanical Metallurgy: Principles and Applications 1984, Prentice-Hall, Inc., Englewood Cliffs, NJ 07632, USA, 1984, p. 761.